

# Gravitational-wave signatures of non-violent non-locality

Brian C. Seymour \* and Yanbei Chen 

TAPIR, Walter Burke Institute for Theoretical Physics,  
California Institute of Technology, Pasadena, CA 91125, USA

(Dated: November 22, 2024)

Measurement of gravitational waves can provide precision tests of the nature of black holes and compact objects. In this work, we test Giddings' non-violent non-locality proposal, which posits that quantum information is transferred via a nonlocal interaction that generates metric perturbations around black holes. In contrast to firewalls, these quantum fluctuations would be spread out over a larger distance range — up to a Schwarzschild radius away. In this letter, we model the modification to the gravitational waveform from non-violent non-locality. We modify the nonspinning EOBNRv2 effective one body waveform to include metric perturbations that are due to a random Gaussian process. We find that the waveform exhibits random deviations which are particularly important in the late inspiral-plunge phase. We find an optimal dephasing parameter for detecting this effect with a principal component analysis. This is particularly intriguing because it predicts random phase deviations across different gravitational wave events, providing theoretical support for hierarchical tests of general relativity. We estimate the constraint on the perturbations in non-violent non-locality with events for the LIGO-Virgo network and for a third-generation network.

**Introduction.** The evaporation of black holes (BHs) via Hawking radiation [1] reveals an inconsistency between quantum mechanics and general relativity (GR) [2]: the semiclassical result that Hawking radiation carries no information contradicts the *unitarity* of quantum theory. Several resolutions to the *information paradox* have been proposed: the BH could never fully decay but remain as a massive remnant [3]. The interior geometry of the BH could be modified as a fuzzball [4] or gravastar [5]. Alternatively, the firewall scenario [6] suggests the region near the horizon could experience a breakdown of semiclassical gravity which destroys infalling observers. Finally, the information paradox may be resolved by accounting for non-perturbative contributions in semiclassical gravity through the replica wormhole trick, which restores unitarity without modifying GR [7–11].

Giddings proposed that the information which fell into the BH can escape it via *non-violent non-locality* (NVNL) [12–15], a non-local interaction between the inside and the outside of the BH, with associated non-violent space-time fluctuations from this information transfer. In the "strong" version of NVNL, space-time metric fluctuate stochastically at a level of  $\mathcal{O}(1)$  [14] near BHs, while the "weak" version [15] has fluctuations of  $\mathcal{O}(e^{-S_{\text{bh}}/2})$  [16]. Giddings and collaborators elaborated the phenomenology of NVNL [17–19] to observations of the Event Horizon Telescope (EHT) [20]. They recently considered scatterings of gravitational waves by BHs [21].

The detection of gravitational waves (GW) allows us to probe directly the behavior of strong gravity around black hole (BH)s and neutron star (NS)s [22–27]. Deviations from GR can be extracted by adopting either the parameterized post-Einsteinian (PPE) framework [28] or the parameterized post-Newtonian (PN) deformation framework [29–31], which measure deviations in the GW phase during the binary inspiral stage. Results of parametrized tests have been featured in LIGO-

Virgo-KAGRA (LVK) results [24–27, 32], which also treated the phase deviation parameters as hyperparameters and bounded their mean values as well as uncertainties [33, 34]. In this letter, we model the effect of NVNL on the inspiral of a binary black hole (BBH) and show that it can be constrained by the parametrized tests mentioned above, in particular via the uncertainties of the phase-deviation hyperparameters [33].

We begin with the effective-one-body (EOB) framework [35, 36] which approximates a two-body relativistic problem as a one-body problem in a deformed Schwarzschild spacetime, the *effective* spacetime. In the EOBNRv2 spacetime [37], we add stochastic metric perturbations characterized by a Gaussian spatial profile and a frequency spectrum related to the BH's temperature, as proposed by Ref. [19] for an isolated BH. The resulting trajectories lead to gravitational waveforms that deviate from GR stochastically, primarily in the late-inspiral and plunge phases. Using a principal component analysis [38–40], we show that the frequency-domain phase deviations of these waveforms can be well approximated by a single dominant eigenmode multiplied by a normally distributed random amplitude. Finally, we estimate how well NVNL can be constrained by stacking together gravitational-wave events and computing the Savage-Dickey ratio [41]. These calculations give theoretical support to search for random phase deviations as proposed in the hierarchical tests of GR [27, 33, 42–45].

**Setup.** For a Schwarzschild BH, Ref. [19] generically decomposes the NVNL-induced metric perturbations  $g_{\mu\nu} = g_{\mu\nu}^s + h_{\mu\nu}$  into the even and odd perturbations [46]. In this work, we will consider the dominant correction which arises from  $h_{vv}$  in the in-going Eddington-Finkelstein coordinates, decomposed as

$$h_{vv} = \sum_{\ell m} f_{\ell m} Y_{\ell m}, \quad (1)$$

where

$$f_{\ell m} = A_{\ell m} \exp \left[ -(r - r_S)^2 / (2r_G^2) \right] n(t), \quad (2)$$

with  $A_{\ell m}$  the amplitude of the mode,  $r_S$  the Schwarzschild radius, and  $r_G \sim r_S$  the localization length of the perturbations [19]. Here  $n(t)$  is a colored Gaussian noise with a power spectrum

$$S_n(f) = 1/(2f_Q) \exp[-|f|/f_Q], \quad (3)$$

where  $f_Q = 1/8\pi M$  is the quantum frequency scale. We have normalized the power spectrum so that  $n(t)$  has a variance equal to unity  $\langle n^2(t) \rangle \equiv \int df S_n(f) = 1$ . This spectrum is motivated by the Boltzman distribution for a BH of temperature  $T_{\text{BH}} = 1/8\pi M$ . Note that the standard deviation of  $f_{\ell m}$  at the horizon is  $\sim A_{\ell m}$ , while the coherence time is around  $\tau \sim 4M$ .

Let us now review the EOB framework [35–37, 47, 48]. We define total mass  $M = m_1 + m_2$ , symmetric mass ratio  $\eta = m_1 m_2 / M^2$ , and mass ratio  $q = m_1 / m_2$ . The effective metric is given by

$$ds_{\text{eff}}^2 = -A(r)dt^2 + \frac{D(r)}{A(r)}dr^2 + r^2 d\Omega^2, \quad (4)$$

where  $A(r) = 1 - \frac{2M}{r} + \mathcal{O}(\eta)$  and  $D(r) = 1 + \mathcal{O}(\eta)$  are terms that describe the effective metric which is deformed by the symmetric mass ratio  $\eta$  away from Schwarzschild. (See the Supplemental Materials for further details.) If we parameterize our metric with coordinates  $\vec{q} = (r, \phi)$  and their conjugate momenta  $\vec{p} = (p_r, p_\phi)$ , the effective Hamiltonian is found with the mass shell condition  $p_\mu p_\nu g_S^{\mu\nu} = -1$

$$\hat{H}_{\text{eff}}^S = \sqrt{A(r) \left( 1 + \frac{p_\phi^2}{r^2} + \frac{A}{D} p_r^2 \right)}. \quad (5)$$

The physical Hamiltonian for the system is related to the effective Hamiltonian via

$$\hat{H}_{\text{real}}^S = \eta^{-1} \sqrt{1 + 2\eta (\hat{H}_{\text{eff}}^S - 1)}, \quad (6)$$

where the hat denotes the Hamiltonian is in dimensionless units. Hamilton's equations are then

$$\frac{dq_i}{dt} = \frac{\partial \hat{H}_{\text{real}}}{\partial p_i}, \quad \frac{dp_i}{dt} = -\frac{\partial \hat{H}_{\text{real}}}{\partial q_i} + \mathcal{F}_i^{\text{rad}}, \quad (7)$$

where the generalized force  $\mathcal{F}_i^{\text{rad}}$  is added to incorporate radiation reaction.

Let us now add NVNL into EOB by modifying the geometry of the effective spacetime, leading to a modified mass-shell relation  $p_\mu p_\nu (g_S^{\mu\nu} + h^{\mu\nu}) = -1$  and yields a modified Hamiltonian

$$\hat{H}_{\text{real}} = \hat{H}_{\text{real}}^S + h_{\nu\nu}^{\ell m} \Delta \hat{H}_{\ell m}^{\text{real}}. \quad (8)$$

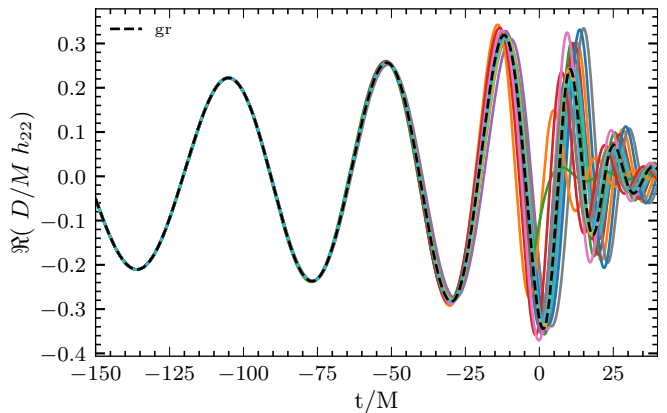


FIG. 1. The real part of the dimensionless  $h_{22}(t)$  strain for  $A_{22} = 5 \times 10^{-2}$ . This is the *full waveform* before the principal component analysis is done, so it contains all perturbations. These signals are aligned at very early times so that their signals overlap at low frequencies but they stochastically diverge as they reach the plunge. The apparent ringdown difference is primarily due to the phenomenological ringdown attachment, but we only do the testing GR analyses with the inspiral piece.

In principle, the gravitational wave luminosity  $\dot{E}$ , hence  $\mathcal{F}_i^{\text{rad}}$  is also modified by NVNL, but we will be focusing on the conservative modifications to the waveform while such effects are analyzed in other works [21]. We obtain the NVNL trajectory  $(q_i(t), p_i(t))$  using Hamiltonian (8) and Eqs. (7). We then obtain the leading quadrupole wave  $h_{22}$  in the same way as Ref. [37], attaching a simple GR ringdown where the strain peaks via smoothness (in a similar manner to [49]). (See Supplemental Materials for details.)

**NVNL Waveforms.** In Fig. 1, we plot several realizations of an NVNL waveform  $\text{Re}[h_{22}]$  (normalized by  $M/D$  with  $D$  the source distance) in the time domain, as functions of  $t/M$ , for a binary with  $q = 1$ , and compare this to a GR waveform. The random deviations are smooth in time due to the cutoff  $f_Q$  in Eq. (3) as well as the filtering effect due to the inertia of the binary.

Going to the frequency domain, the NVNL waveform at linear order in  $A_{\ell m}$  can be approximated by

$$h(f; \theta, A_{\ell m}) = h_{\text{gr}}(\theta) e^{i \sum_{\ell m} \Delta \Psi_{\ell m}(f; \theta)}, \quad (9)$$

with  $\Delta \Psi_{\ell m}(f) \propto A_{\ell m}$  a stochastic phase deviation from GR.  $\Delta \Psi_{\ell m}(f)$  is found by simulating a NVNL waveform with metric fluctuations  $n_i(t)$  in the time domain and taking the Fourier transform for a particular noise realization.

Since our metric deviations are Gaussian, the deviation in the frequency domain is just the metric deviations multiplied by a transfer function. In Fig. 2, one can see the frequency domain phase deviations for various noise realizations. Notice that the frequency domain phase is primarily a stochastic deviation rather than having a secular effect that is com-

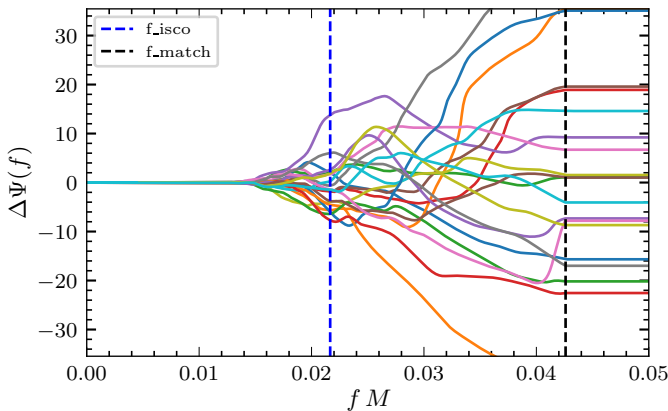


FIG. 2. Frequency domain phase deviation realizations for  $A_{22} = 1$ . Using time domain waveform realizations shown in Fig. 1, we plot the amount of dephasing from GR that they will have. We also plot the frequency at which the binary crosses the inner most stable circular orbit (dashed blue) and the frequency at which the inspiral portion of the waveform is matched to the ringdown (dashed black). Note that  $A_{22} = 1$  is not a small deviation from GR, so we calculated this at  $A_{22} \ll 1$  and scaled it appropriately. One can see that the secular effect of NVNL is nearly zero while the theory predicts random dephasing from GR.

mon to all these noise realizations. Let us define the quantity  $\mu_{\ell m} \equiv \langle \Delta\Psi_{\ell m}(f) \rangle$  and  $\Sigma_{\ell m}(f, f') = \langle (\Delta\Psi_{\ell m}(f) - \mu_{\ell m}(f))(\Delta\Psi_{\ell m}(f') - \mu_{\ell m}(f')) \rangle$ . For this problem, the mean deviation is very small compared to the variance so detection hinges on finding the presence of  $\Sigma_{\ell m}$ .

We can make the waveform template in Eq. (9) more tractable by performing a principal component analysis (PCA). This corresponds to diagonalizing the covariance matrix

$$\Sigma_{\ell m}(f, f') = \sum_k (\sigma_{\ell m}^k)^2 z_{\ell m}^k(f) z_{\ell m}^k(f'), \quad (10)$$

where  $(\sigma_{\ell m}^k)^2$  is the  $k$ th largest eigenvalue and  $z_{\ell m}^k(f)$  its corresponding eigenvector. The PCA is performed for  $f_{\text{start}} < f < f_{\text{match}}$  where  $f_{\text{start}} = 0.004$  and  $f_{\text{match}} = 0.042/M^1$ . As it turns out, for a nearly equal mass ratio, using a single component is able to capture more than 94% of the total variance. If we only include the largest principal component

$$h(f; \theta, A_{\ell m}) = h_{\text{gr}}(\theta) e^{i \sum_{\ell m} \zeta_{\ell m} z_{\ell m}(f)}, \quad (11)$$

where  $\zeta_{\ell m} \sim \mathcal{N}(\mu_{\ell m}, \sigma_{\ell m})$  and we dropped the  $k = 0$  index; we further scale the eigenvectors so that  $\sigma_{\ell m} =$

<sup>1</sup> Note that the output of the dominant PCA eigenvector is completely equivalent to finding  $\min_z \sum_{ij} (\Sigma(f_i, f_j) - z(f_i)z(f_j))^2$  with constant norm.

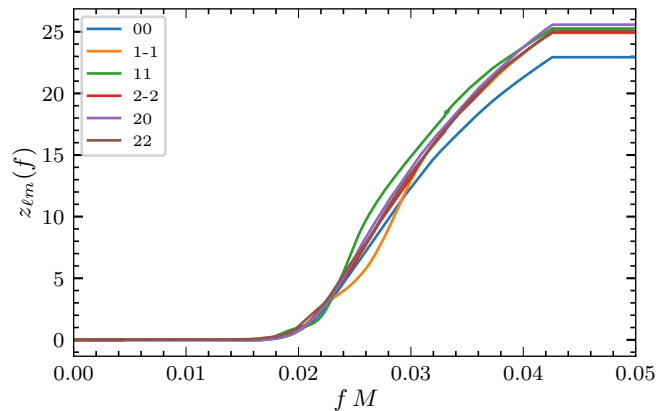


FIG. 3. The largest principal component modes of the covariance matrix. All modes with odd  $l + m$  are zero since we are confined to the orbital plane with  $\theta = \pi/2$ . The largest eigenvector accounts for  $\sim 94\%$  of the phase variance of all modes. One can see that similar deviations happen for all  $(\ell, m)$  modes.

$A_{\ell m}$ , and note that  $\mu_{\ell m}/\sigma_{\ell m} \ll 1$ . In Fig. 3, we plot  $z_{\ell m}(f)$  for each mode up to  $l = 2$ . Since the profile of these curves looks very similar, we will only search for the  $(\ell, m) = (2, 2)$  case and neglect the  $(\ell, m)$  labeling henceforth. We stress that we apply PCA directly to the NVNL theory itself, rather than in the measurement space, which is the usual approach in the literature [38–40]. See Supplemental Materials for further details of the PCA.

**Extraction of NVNL from data.** Next, we describe how well hyperparameters  $(\mu, \sigma)$  can be estimated from a collection of GW events. Each  $\zeta$  realization is drawn from the true distribution  $\mathcal{N}(\mu_t = 0, \sigma_t = A)$ .

For events with high signal-to-noise ratio (SNR), parameter estimation accuracy can be quantified by the Fisher information matrix [50], defined as

$$\Gamma_{IJ} = (\partial_I h(\Theta^I) | \partial_J h(\Theta^J)). \quad (12)$$

Here we have parametrized the GW signal  $h$  with parameters  $\Theta^I = (\theta^i, \zeta)$ , where  $\theta^i$  are GR parameters and  $\zeta$  is the NVNL deviation parameter. The noise-weighted inner product is defined as

$$(g | h) = 4 \text{Re} \int_0^\infty \frac{\tilde{g}^*(f) \tilde{h}(f)}{S(f)} df, \quad (13)$$

Given data  $d$  (which contains a high SNR signal) from a single event, the likelihood function for its parameters  $\Theta$  can be written as

$$p(d|\Theta) = \sqrt{\frac{\det \Gamma}{(2\pi)^{n_\Theta}}} \exp \left[ -\frac{1}{2} (\Theta_I - \Theta_I^{\text{ML}}) \Gamma_{IJ} (\Theta_J - \Theta_J^{\text{ML}}) \right], \quad (14)$$

where we have used  $\Theta_J^{\text{ML}}$  to denote the values of  $\Theta_J$  where likelihood is maximized and  $n_\Theta$  is the number of

entries of  $\Theta_I$ . In a frequentist approach, we can use  $\Theta_I^{\text{ML}}$  as the Maximum Likelihood Estimator (MLE) for signal parameters. Given a large number of trials with true parameters  $\Theta_I^t$ , we can denote  $\delta\Theta_I = \Theta_I^{\text{ML}} - \Theta_I^t$ . For high SNR,  $\delta\Theta_I$  is a Gaussian random vector with  $\langle \delta\Theta_I \delta\Theta_J \rangle = (\Gamma^{-1})_{IJ}$ . In particular, marginalizing over  $\theta_i$ , the MLE estimator  $\zeta^{\text{ML}}$  has an error of  $\langle \delta\zeta^2 \rangle = (\Gamma^{-1})_{\zeta\zeta} \equiv \Delta\zeta^2$ .

Let us take a quick aside and discuss how the generic PN deformation tests [28–30] would capture the effects of NVNL in the waveform. This can still be done by standard techniques for biased waveform models [51, 52]. We fully derive this in [53], but here is an abbreviated version of the derivation. A  $n$ th order dephasing template has the form

$$\Delta\Psi_n = \frac{3}{128\eta} \varphi_n \delta\varphi_n (\pi M f)^{(n-5)/3}, \quad (15)$$

which is same convention as the LVK GWTC3 testing GR paper [27]. If we inject a  $\zeta^t$ , and try to measure  $\Theta^I = (\theta^i, \delta\varphi_n)$ , we would find that the maximum likelihood estimator is

$$\Gamma_{IJ} \begin{pmatrix} \theta_i^{\text{ML}} - \theta_i^t \\ \delta\varphi_n^{\text{ML}} \end{pmatrix} = \begin{pmatrix} (\partial_{\theta^i} h | i \Delta\Psi_{\text{NVNL}} h_{\text{gr}}) \\ (\partial_{\delta\varphi_n} h | i \Delta\Psi_{\text{NVNL}} h_{\text{gr}}) \end{pmatrix} + \begin{pmatrix} (\partial_{\theta^i} h | n) \\ (\partial_{\delta\varphi_n} h | n) \end{pmatrix}. \quad (16)$$

This means that  $\delta\varphi_n^{\text{ML}} = \Sigma_{\delta\varphi_n, J} (\partial_J h | i z(f) h_{\text{gr}}) \zeta^t$  with an uncertainty that comes from covariance matrix  $\Sigma_{IJ} = (\Gamma^{-1})_{IJ}$ . Thus for a small bias, the maximum likelihood point is shifted, but the statistical uncertainty is given by the Fisher matrix calculated with the parameterized test parameters  $(\theta_i, \delta\varphi_n)$ . In Ref. [53], we prove this fully and ascribe geometric meaning to how deviations are captured by parameterized PN templates.

Let us now construct a hierarchical analysis for the distribution of the  $\zeta$  parameter for a collection of events, in a similar manner to how the LVK does [27]. We model  $\zeta$  as  $\zeta \sim \mathcal{N}(\mu, \sigma)$  and would like to estimate the posterior on the hyperparameters  $(\mu, \sigma)$ . For event  $a$ , we write

$$\begin{aligned} p(d_a | \mu, \sigma) &= \int d\zeta p(d_a | \zeta) p(\zeta | \mu, \sigma), \\ &= \frac{1}{\sqrt{2\pi} \sqrt{\Delta\zeta_a^2 + \sigma^2}} \exp \left[ -\frac{1}{2} \frac{(\zeta_a^{\text{ML}} - \mu)^2}{\Delta\zeta_a^2 + \sigma^2} \right], \end{aligned} \quad (17)$$

where  $\zeta_a^{\text{ML}}$  and  $\Delta\zeta_a$  are the MLE estimator and parameter uncertainty for  $\zeta$  obtained from this event. Note that the maximum likelihood point for event  $a$  has the distribution

$$\zeta_a^{\text{ML}} \sim \mathcal{N} \left( 0, \sqrt{\sigma_t^2 + \Delta\zeta_a^2} \right), \quad (18)$$

which follows from  $\zeta_a^t \sim \mathcal{N}(0, \sigma_t)$  and  $\zeta_a^{\text{ML}} \sim \mathcal{N}(\zeta_a^t, \Delta\zeta_a)$ . If a generic PN test were performed instead, the maximum likelihood point is distributed like

$$\delta\varphi_{n,a}^{\text{ML}} \sim \mathcal{N} \left( 0, \sqrt{\alpha_a^2 \sigma_t^2 + (\Delta\delta\varphi_{n,a})^2} \right), \quad (19)$$

since  $\delta\varphi_{n,a}^{\text{ML}} \sim \mathcal{N}(\alpha_a \zeta^t, \Delta\delta\varphi_{n,a})$  where  $\alpha_a \equiv \Sigma_{\delta\varphi_n, I} (\partial_I h | i z(f) h_{\text{gr}})$  is the coupling for event  $a$  given by Eq. (16). The entire collection of events leads to the joint likelihood

$$p(\{d_a\} | \mu, \sigma) = \prod_{a=1}^N p(d_a | \mu, \sigma), \quad (20)$$

where  $(\mu, \sigma)$  are the hyper parameters for  $\zeta$ , but the framework works analogously for PN deformation hyperparameters  $(\mu_n, \sigma_n)$ . The number of events is  $N$ , and we do not include corrections for selection effects [54] or the probability of obtaining  $N$  events [43, 55]. To compute the consistency with GR, we use Bayes factors which compare the support for or against GR. Since we are comparing nested a nested model where GR is a single point  $(0, 0)$  in the  $(\mu, \sigma)$  plane, it becomes the well known Savage-Dickey ratio [41]. The Bayes factor  $\mathcal{B}$  is defined to be the ratio of the evidences

$$\log \mathcal{B}_{\text{GR}}^{\text{bGR}} = \log \left( \frac{p(d | \text{bGR})}{p(d | \text{GR})} \right) = \log \left( \frac{p(0, 0 | d, \text{bGR})}{p(0, 0 | \text{bGR})} \right), \quad (21)$$

where we are using the notation  $p(x | d, M)$  to represent the posterior probability density  $x$  given data  $d$  under modeling assumptions  $M$ . One can see that the Savage-Dickey ratio compares how much the posterior has changed to the prior at the location of the GR limit. We use priors which are uniform in the range of  $-1 \leq \mu \leq 1$  and  $0 \leq \sigma \leq 1$ .

Next, we investigate how detectability the effects of NVNL are if it were injected in the data. In Fig. 4 we show a contour plot of the Savage-Dickey ratio for a three detector network Livingston-Hanford-Virgo at O3 Livingston sensitivity. In particular, we calculate the Fisher information matrix for five years of events where we draw from the astrophysical rates. The merger rate density scales with the star formation rate and the masses are drawn from the POWER LAW+PEAK (PP) model [56, 57] that is the best fit point from GWTC3 data [58]. We measure both the event parameters and the testing GR parameter and marginalize over the event parameters. We perform this analysis for the optimal principal component dephasing term. Additionally, we give the results for the traditional PN deformation coefficients based upon the biased framework [53]. We can see that NVNL can be constrained such that  $A \lesssim 6 \times 10^{-3}$  after five years of observation at O3 sensitivities when using the PCA method  $\zeta$ . The 3.5PN dephasing term,  $\delta\varphi_7$ , performed the best out of the parameterized tests and found the constraint  $A \lesssim 7 \times 10^{-3}$ . The minimum detectable value doesn't strongly depend on which PN order you use, but the PCA method was optimal. This is consistent with previous work showing that deviations are detectable with most PN tests [59, 60].

We perform the same analysis for the case of third generation gravitational wave detectors. We consider three

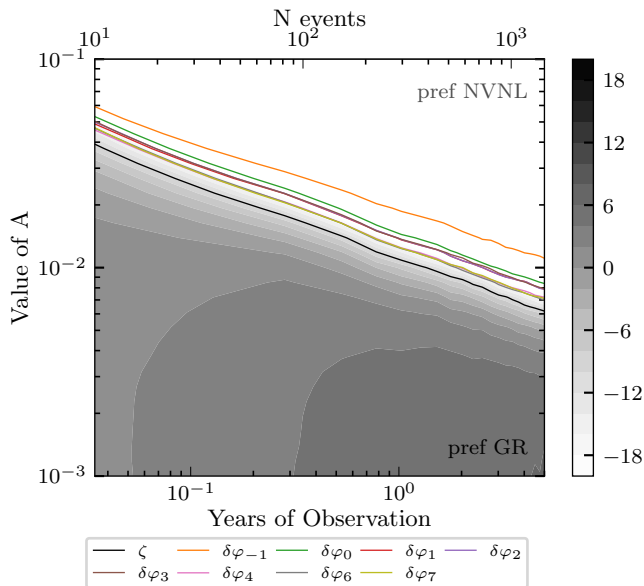


FIG. 4. The log Bayes factor projected constraint for Hanford-Livingston-Virgo network operating at O3 Livingston sensitivity (positive favors GR). We plot this for various values of  $A$  and for increasing numbers of events. The line corresponding to  $-10 \log$  Bayes factor is shown for the optimal PCA model (black) and PN coefficients (other colors) where GR is disfavored. Using an event list, we perform parameter estimation for five years of detectable events and then compute the Bayes factor for the hierarchical test of GR. Note that the PCA model is best able to constrain the effects of NVNL most stringently, but the PN coefficients are able to detect a violation of  $A \neq 0$  nearly as well. We also see that the largest PN orders perform the best. For a five year observation, the bound for the PCA model is  $A < 6.2 \times 10^{-3}$ .

Cosmic Explorer detectors located at the locations of the current LIGO/Virgo network. With this improvement in sensitivity, we see that the five year constraint on  $A$  is  $A \lesssim 4 \times 10^{-4}$  for the PCA method and  $A \lesssim 5 \times 10^{-4}$  for the 3.5PN parameterized test, as shown in Fig. 5. For both of these cases, we produced the figure by re-sampling over many realizations of events and their associated noise realization so that very loud events do not show drastic shifts in the constraint. In the supplemental material, we show much the variance of the log Bayes factor versus observation time.

To perform our analysis on actual data, we need to take the further step making an NVNL-EOB model which includes spin effects and is properly calibrated to numerical relativity waveforms, for example with SEOBNRv5 [49].

**Conclusion.** In this work, we have modeled the effects of non-violent non-locality for a binary black hole merger and estimated how well this can be measured in current and third generation detectors. By incorporating NVNL fluctuations to an EOB model, we obtained modified trajectories for the binary, and the corresponding

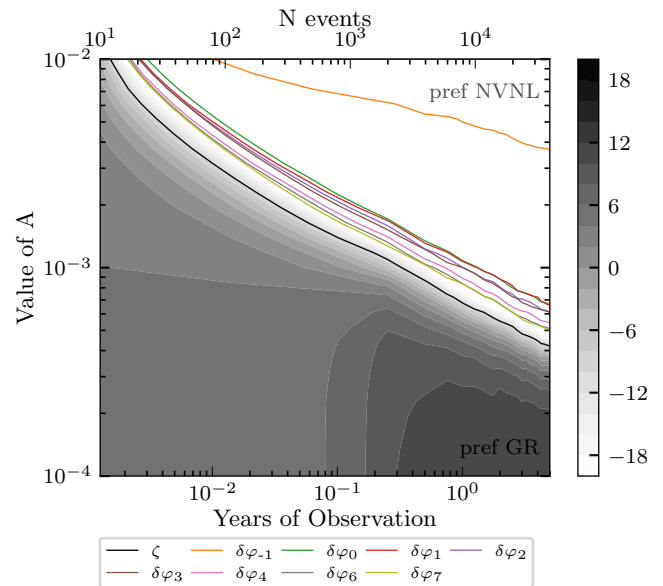


FIG. 5. The log Bayes factor for the Hanford-Livingston-Virgo network operating at CE sensitivity (positive favors GR). This plot shows the same scaling as Fig. 4, but contains more events since CE detects more in a five year period. For a five year observation, the bound for the PCA model is  $A < 4.2 \times 10^{-4}$ .

gravitational waveforms. These waveforms' phase deviation from GR in the frequency domain can be well approximated as a single mode function times a random coefficient with normal distribution with zero mean and standard deviation  $A$ , which in turn also characterizes the typical size of the metric perturbations close to the horizon. We estimated constraints that can be posed by LVK and third-generation detectors. To perform our analysis on actual data, we need to take the further step making an NVNL-EOB model which includes spin effects and is properly calibrated to numerical relativity waveforms, for example with SEOBNRv5 [49].

Our work has been limited to conservative dynamics during the inspiral stage. To obtain a more complete picture of NVNL effects, one should: (i) combine our work with Ref. [21] to incorporate NVNL's modifications to radiation reaction during the inspiral stage, and (ii) model the effect of NVNL perturbations on wave propagation through the final BH's spacetime in order to capture how the ringdown waves will be modified.

**Acknowledgments.** We thank Jacob Golomb, Ethan Payne, Sophie Hourihane, Max Isi, Bangalore Sathyaprakash, Matthew Giesler, Steve Giddings, Hang Yu, and Katerina Chatziioannou for their insightful discussions. B.S. acknowledges support by the National Science Foundation Graduate Research Fellowship under Grant No. DGE-1745301. Y.C. and B.S. acknowledge support from the Brinson Foundation, the Simons

Foundation (Award Number 568762), and by NSF Grants PHY-2011961, PHY-2011968, PHY-1836809.

### Supplemental Material

**EOB Waveform.** We made our EOB waveform by

$$\hat{H}^{\text{eff}}(r, \phi, p_r, p_\phi) = \frac{g^{0i} p_i}{g^{00}} + \sqrt{\frac{1 + g^{ij} p^i p^j}{-g^{00}} + \left(\frac{g^{0ri} p_i}{g^{00}}\right)^2 + \frac{Q(p^4)}{-g^{00}}}. \quad (22)$$

where the modification to the mass shell is  $Q(p^4) = 2\eta(4 - 3\eta)p_r^4$  which we do not modify due to NVNL since it is a high PN order effect. By perturbing  $g^{\mu\nu}$  in Eq. (22), we find the perturbation to the real Hamiltonian  $\Delta\hat{H}^{\ell m}$

$$\hat{H}_{\text{real}} = \hat{H}_{\text{real}}^{\text{S}} + h_{vv}^{\ell m} \Delta\hat{H}_{\ell m}^{\text{real}}. \quad (23)$$

In this section, we will be using dimensionless units so  $t = T/M$ ,  $r = R/M$ ,  $p_r = P_R/M$ , and  $p_\phi = P_\phi/(M\mu)$ . The equations of motion for the EOB trajectory are found by solving Hamilton's equations with radiation reaction terms. If we explicitly write out the EOB trajectory evolution equations with the perturbations we have

$$\begin{aligned} \frac{\partial r}{\partial t} &= \frac{\partial \hat{H}_{\text{real}}^{\text{S}}}{\partial p_r} + \frac{\partial \Delta\hat{H}_{\ell m}^{\text{real}}}{\partial p_r} h_{vv}^{\ell m}, \\ \frac{\partial \phi}{\partial t} &= \hat{\omega} = \frac{\partial \hat{H}_{\text{real}}^{\text{S}}}{\partial p_\phi} + \frac{\partial \Delta\hat{H}_{\ell m}^{\text{real}}}{\partial p_\phi} h_{vv}^{\ell m}, \\ \frac{\partial p_r}{\partial t} &= -\frac{\partial \hat{H}_{\text{real}}^{\text{S}}}{\partial r} + \hat{\mathcal{F}}_\phi \frac{p_r}{p_\phi} - \frac{\partial (\Delta\hat{H}_{\ell m}^{\text{real}} h_{vv}^{\ell m})}{\partial r}, \\ \frac{\partial p_\phi}{\partial t} &= \hat{\mathcal{F}}_\phi - \frac{\partial (h_{vv}^{\ell m})}{\partial \phi} \Delta\hat{H}_{\ell m}^{\text{real}}, \end{aligned} \quad (24)$$

and the  $\phi$  component of the radiation-reaction force is

$$\hat{\mathcal{F}}_\phi = -\frac{1}{\eta v_\omega^3} \frac{dE}{dt}, \quad (25)$$

where  $v_\omega = \hat{\omega}^{1/3}$ . The GW luminosity is generally

$$\frac{dE}{dt} = \frac{v_\omega^6}{8\pi} \sum_{\ell=2}^{\infty} \sum_{m=\ell-2}^{\ell} m^2 \left| \frac{D_L}{M} h_{\ell m} \right|^2, \quad (26)$$

however we make the approximation and only include the (2, 2) mode. To construct  $h_{22}(t)$ , we are using the Newtonian contribution as given in Eq. (16) of [37]. It is equal to

$$h_{22} = -\frac{32\pi}{5} \sqrt{\frac{2}{3}} \frac{M\eta}{D_L} v_\phi^2 Y^{2-2} \left( \frac{\pi}{2}, \phi \right), \quad (27)$$

modifying the nonspinning EOBNRv2 waveform [37]. Given an effective metric, one can solve for the effective Hamiltonian by solving the mass-shell constraint  $p_\mu p_\nu g^{\mu\nu} = -1 - Q(p^4)$

where

$$v_\phi \equiv \hat{\omega} r_\omega \equiv \hat{\omega} r [\psi(r, p_\phi)]^{1/3}, \quad (28)$$

and

$$\psi(r, p_\phi) = \frac{2 \left\{ 1 + 2\eta \left[ \sqrt{A(r) \left( 1 + p_\phi^2/r^2 \right)} - 1 \right] \right\}}{r^2 dA(r)/dr}. \quad (29)$$

Since our analysis is focusing on how the waveform differs by adding metric perturbations away from GR, we neglected to include various calibration terms that are included in EOBNRv2. In Ref. [37], they use the factorized resummed modes [48, 61, 62] which include corrections to the Newtonian modes motivated from numerical relativity. Specifically, we use  $h_{\ell m}^F = h_{\ell m}^N$  in Eq. (14) of [37]. We also do not include the effects of the non-quasicircular orbit coefficients in Eq. (13) of [37].

We attach a phenomenological ringdown to our waveform. Since we didn't include the GR calibration from the non-quasicircular orbit coefficients, we found that it was hard to get a good fit with the comb approach used in [37]. This is because the quasinormal modes are at a much higher frequency than the gravitational wave frequency at the merger-ringdown fit point. Without properly fitting to NR, we saw a preference for unphysical second peaks similar to what is shown in Fig. 3 of [37]. Instead, we choose the fit location  $\partial_t |h_{22}| = 0$  and attach a ringdown. If we write the  $h_{22}$  waveform as

$$h_{22}(t) = A_{22}(t) e^{-i\phi_{22}(t)}, \quad (30)$$

where time is scaled so that merger happens  $t = 0$ . The phenomenological ringdown waveform is described by

$$\omega_{22, \text{RD}}^r(t) = \omega_{220}^r \left( 1 - \sum_{i=1}^2 \alpha_i e^{-t/\tau_i} \right), \quad (31)$$

and the ringdown amplitude is

$$A_{22, \text{RD}}(t) = A_{22}|_{t=0} \exp \left[ \omega_{220}^i t \left( 1 + \sum_{i=1}^2 \beta_i e^{-t/\tau_i} \right) \right], \quad (32)$$

where  $\omega_{220} = \omega_{220}^r + i\omega_{220}^i$ . We set  $\alpha_i$  and  $\beta_i$  by enforcing that the match between inspiral and ringdown is twice continuously differentiable  $h'_{22,\text{IM}}(t) = h'_{22,\text{RD}}(t)$  and  $h''_{22,\text{IM}}(t) = h''_{22,\text{RD}}(t)$ . We note that the accuracy of the ringdown fit isn't that important because we are only searching for deviations from GR during the inspiral-merger and assume  $\Delta\Psi(f)$  is constant after merger (as can be seen in Fig. 2 above  $Mf \sim 0.4$ ). Our analysis of NVNL in the ringdown phase is part of an ongoing future work.

**Accuracy of PCA.** Let us now discuss the accuracy of the PCA. We do this by comparing the variance in the phase deviation that is captured by our PCA model to the full phase deviation. We find the full dephasing by computing a FFT  $\Delta\Psi_{\text{full}}(f)$  and the PCA dephasing is  $\Delta\Psi_{\text{PCA}}(f) = \zeta z(f)$  where  $z(f)$  is the most dominant principal mode and  $\zeta$  is a parameter so that  $|\Delta\Psi_{\text{full}}(f) - \Delta\Psi_{\text{PCA}}(f)|$  is minimized. The variance captured at each frequency  $f$  by the PCA is

$$\begin{aligned} \sigma_{\Delta\Psi}^{\text{est}}(f) &\equiv \frac{\langle \Delta\Psi_{\text{PCA}}(f) \Delta\Psi_{\text{full}}(f) \rangle}{\sqrt{\langle \Delta\Psi_{\text{PCA}}^2(f) \rangle}}, \\ &= \frac{\langle \zeta \Delta\Psi_{\text{full}}(f) \rangle}{\sqrt{\langle \zeta^2 \rangle}}. \end{aligned} \quad (33)$$

This needs to be compared to total amount of variance in the full waveform

$$\sigma_{\Delta\Psi}^{\text{tot}}(f) = \sqrt{\langle \Delta\Psi_{\text{full}}^2(f) \rangle}. \quad (34)$$

In Fig. 6, we compare these variance indicators and see the fit quality. One can see that the variance captured by the PCA estimator  $\Psi_{\text{PCA}}(f)$  is less than the true variance in  $\Delta\Psi_{\text{full}}(f)$ , however it does a good job of estimating the variance at high frequencies when the dephasing is largest. Note that the reason that these don't perfectly match up is that the PCA is optimizing the quantity  $|\Sigma(f, f') - \sigma^2 z(f) z(f')|$ . The off diagonal elements of  $\Sigma(f, f')$  where  $f \neq f'$  are better fit by choosing  $z(f)$ .

**Variance of Bayes Factor.** As we noted in the discussion of Fig. 4 and Fig. 5, the Bayes factor measurement depends on randomness about the event order. In Fig. 7, we plot how the (log) Bayes Factor ratio scales for multiple injection sizes of  $A$ . In the center, we show the median Bayes factor for each injection size while the upper and lower bounds are  $\pm 1\sigma$  percentile values for the Bayes factor after this many observations. This mostly occurs because the loudest events are the most informative, so the order of events can affect the rolling constraint. Furthermore, the statistical realization of the detector noise and hierarchical model draw add subdominant variations to the Bayes factor.

**Measuring  $A$ .** While in the main text of this letter, we primarily focused on null tests of NVNL, one can directly measure the size of the deviations. In the same manner that we did before, we can compute the event posteriors for many events and then compute the posterior in

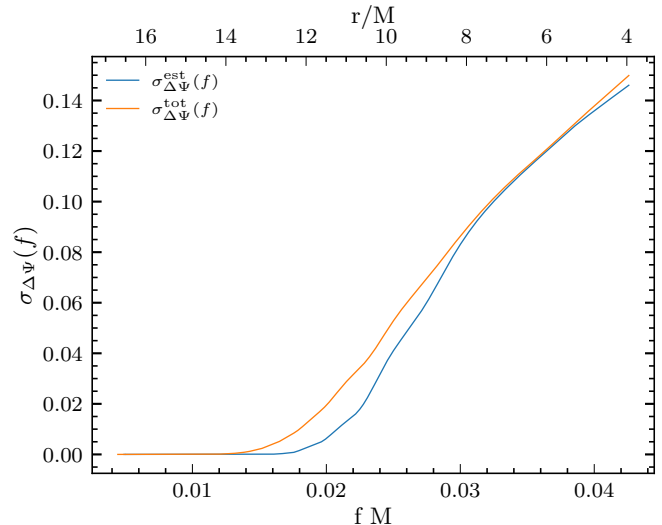


FIG. 6. Comparison of how much variance is captured by the PCA estimator. We see that the full  $\Delta\Psi$  is well described by this. While some of the variance is not captured at low frequencies, at high frequencies there is a nearly perfect match. We plot this for  $A = 6 \times 10^{-3}$  which was the estimated constraint for O3 detectors.

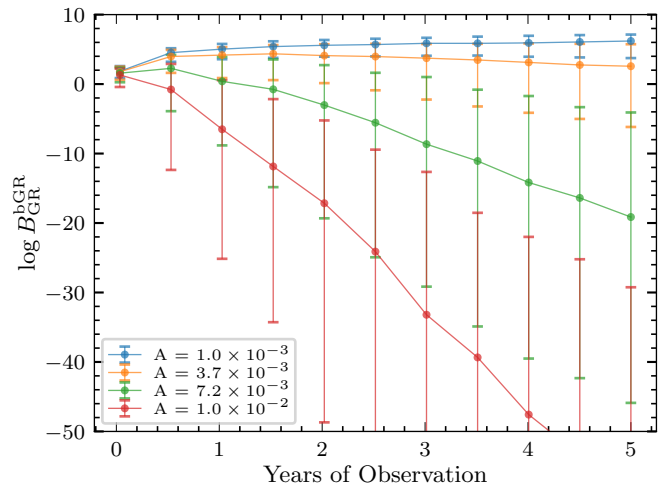


FIG. 7. The log Bayes factor for the Hanford-Livingston-Virgo network at O3 Livingston sensitivity (positive favors GR). One can see that the red curve favors NVNL at large events, while blue favors GR. The whiskers correspond to the upper and lower bounds are  $\pm 1\sigma$  percentile values due to randomness associated with the order of events. If one sees a loud clear event early, then it is easier to favor/disfavor GR.

the hierarchical model. The true value of NVNL parameter  $A$  is for the choice of  $p(\mu, \sigma|d) = p(0, A|d)$ . We can thus compute the confidence interval on  $A$  by finding the maximum posterior location and shade the interval which contains  $1\sigma$  and  $2\sigma$  of the posterior support. We do this for a LIGO-Virgo network at O3 Livingston sensitivity in

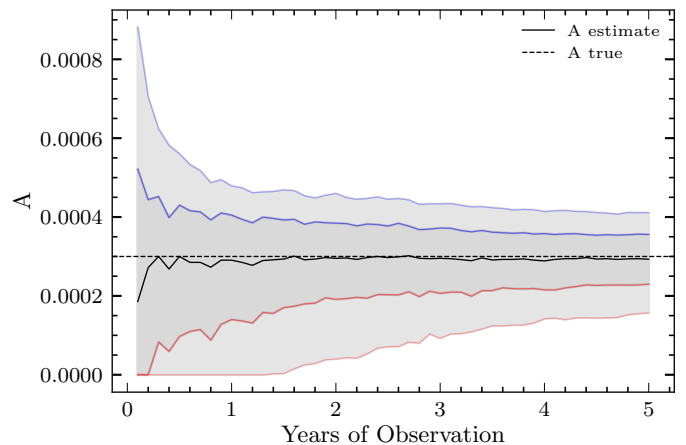
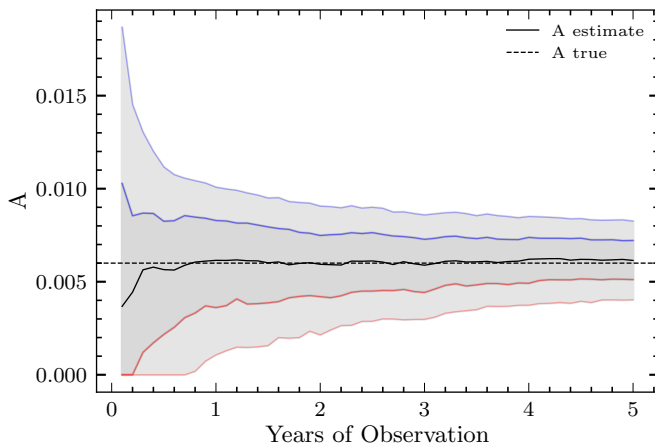
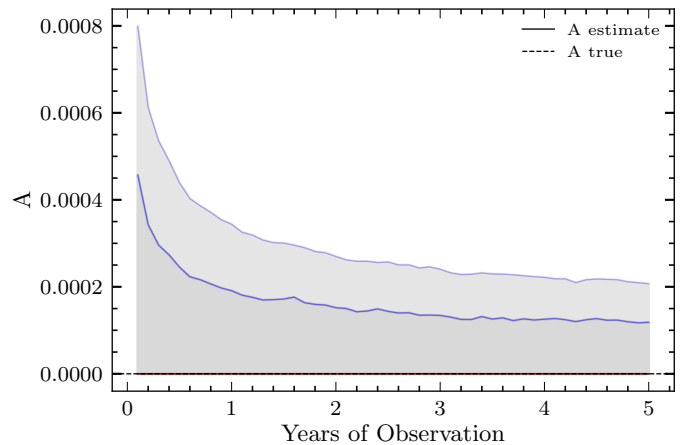
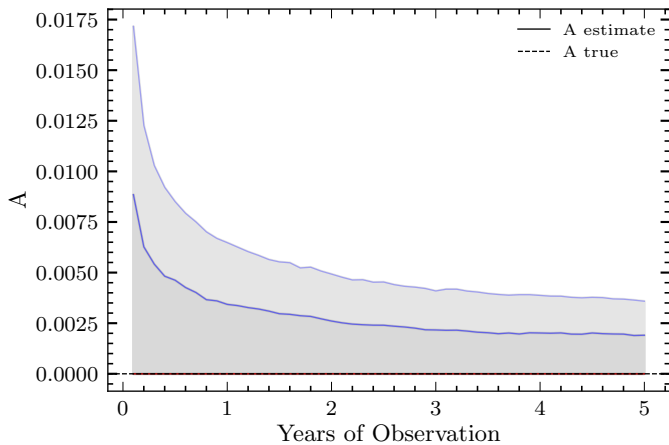


FIG. 8. We show the running estimate of  $A$  for an O3 network. In the top plot, we show the  $1\sigma$  and  $2\sigma$  confidence region when we inject  $A_t = 0$ . We can see that the error shrinks as events are observed. In the bottom plot, we inject  $A_t = 6 \times 10^{-3}$ , and one can see that as events are observed the probability density narrows and detects a violation.

FIG. 9. We show the running estimate of  $A$  for the CE network in an analogous manner of Fig. 8. On the top, we inject  $A_t = 0$ , and on the bottom  $A_t = 3 \times 10^{-4}$ . One can see that as more observations are made, the confidence region begins to exclude  $A = 0$ .

Fig. 8, where on the top is an injection of  $A_t = 0$ , and the bottom has  $A_t = 6 \times 10^{-3}$ . We shade the  $\pm 1\sigma$  and  $\pm 2\sigma$  regions of the posterior as a function of the years of observation. One can see that the case of zero injection slowly asymptotes to a stronger constraint on  $A$  while injection a nonzero  $A$  the credible interval eventually detects it at 95% level after a little less than a year. In Fig. 9, we plot the same case for CE with  $A_t = 3 \times 10^{-4}$ . One can see similar features where the constraint narrows down to the true value as the network observes more events.

\* [seymour.brianc@gmail.com](mailto:seymour.brianc@gmail.com)

- [1] S. W. Hawking, Particle Creation by Black Holes, *Commun. Math. Phys.* **43**, 199 (1975), [Erratum: *Commun. Math. Phys.* 46, 206 (1976)].
- [2] S. W. Hawking, Breakdown of Predictability in Gravitational

tional Collapse, *Phys. Rev. D* **14**, 2460 (1976).

- [3] S. B. Giddings, Black holes and massive remnants, *Phys. Rev. D* **46**, 1347 (1992), [arXiv:hep-th/9203059](https://arxiv.org/abs/hep-th/9203059).
- [4] S. D. Mathur, The Fuzzball proposal for black holes: An Elementary review, *Fortsch. Phys.* **53**, 793 (2005), [arXiv:hep-th/0502050](https://arxiv.org/abs/hep-th/0502050).
- [5] P. O. Mazur and E. Mottola, Gravitational vacuum condensate stars, *Proc. Nat. Acad. Sci.* **101**, 9545 (2004), [arXiv:gr-qc/0407075](https://arxiv.org/abs/gr-qc/0407075).
- [6] A. Almheiri, D. Marolf, J. Polchinski, and J. Sully, Black Holes: Complementarity or Firewalls?, *JHEP* **02**, 062, [arXiv:1207.3123 \[hep-th\]](https://arxiv.org/abs/1207.3123).
- [7] A. Almheiri, N. Engelhardt, D. Marolf, and H. Maxfield, The entropy of bulk quantum fields and the entanglement wedge of an evaporating black hole, *JHEP* **12**, 063, [arXiv:1905.08762 \[hep-th\]](https://arxiv.org/abs/1905.08762).
- [8] A. Almheiri, R. Mahajan, J. Maldacena, and Y. Zhao, The Page curve of Hawking radiation from semiclassical geometry, *JHEP* **03**, 149, [arXiv:1908.10996 \[hep-th\]](https://arxiv.org/abs/1908.10996).
- [9] G. Penington, S. H. Shenker, D. Stanford, and Z. Yang, Replica wormholes and the black hole interior, *JHEP* **03**,



- 205, [arXiv:1911.11977 \[hep-th\]](#).
- [10] A. Almheiri, T. Hartman, J. Maldacena, E. Shaghoulian, and A. Tajdini, Replica Wormholes and the Entropy of Hawking Radiation, *JHEP* **05**, 013, [arXiv:1911.12333 \[hep-th\]](#).
- [11] A. Almheiri, T. Hartman, J. Maldacena, E. Shaghoulian, and A. Tajdini, The entropy of Hawking radiation, *Rev. Mod. Phys.* **93**, 035002 (2021), [arXiv:2006.06872 \[hep-th\]](#).
- [12] S. B. Giddings, Models for unitary black hole disintegration, *Phys. Rev. D* **85**, 044038 (2012), [arXiv:1108.2015 \[hep-th\]](#).
- [13] S. B. Giddings, Nonviolent nonlocality, *Phys. Rev. D* **88**, 064023 (2013), [arXiv:1211.7070 \[hep-th\]](#).
- [14] S. B. Giddings, Modulated Hawking radiation and a non-violent channel for information release, *Phys. Lett. B* **738**, 92 (2014), [arXiv:1401.5804 \[hep-th\]](#).
- [15] S. B. Giddings, Nonviolent unitarization: basic postulates to soft quantum structure of black holes, *JHEP* **12**, 047, [arXiv:1701.08765 \[hep-th\]](#).
- [16] S. B. Giddings, The deepest problem: some perspectives on quantum gravity (2022), [arXiv:2202.08292 \[hep-th\]](#).
- [17] S. B. Giddings, Possible observational windows for quantum effects from black holes, *Phys. Rev. D* **90**, 124033 (2014), [arXiv:1406.7001 \[hep-th\]](#).
- [18] S. B. Giddings, Gravitational wave tests of quantum modifications to black hole structure – with post-GW150914 update, *Class. Quant. Grav.* **33**, 235010 (2016), [arXiv:1602.03622 \[gr-qc\]](#).
- [19] S. B. Giddings and D. Psaltis, Event Horizon Telescope Observations as Probes for Quantum Structure of Astrophysical Black Holes, *Phys. Rev. D* **97**, 084035 (2018), [arXiv:1606.07814 \[astro-ph.HE\]](#).
- [20] K. Akiyama *et al.* (Event Horizon Telescope), First Sagittarius A\* Event Horizon Telescope Results. I. The Shadow of the Supermassive Black Hole in the Center of the Milky Way, *Astrophys. J. Lett.* **930**, L12 (2022), [arXiv:2311.08680 \[astro-ph.HE\]](#).
- [21] K. Fransen and S. B. Giddings, Gravitational wave signatures of departures from classical black hole scattering, *Phys. Rev. D* **110**, 064029 (2024), [arXiv:2405.05970 \[gr-qc\]](#).
- [22] B. P. Abbott *et al.* (LIGO Scientific, Virgo), Observation of Gravitational Waves from a Binary Black Hole Merger, *Phys. Rev. Lett.* **116**, 061102 (2016), [arXiv:1602.03837 \[gr-qc\]](#).
- [23] B. P. Abbott *et al.* (LIGO Scientific, Virgo), GW170814: A Three-Detector Observation of Gravitational Waves from a Binary Black Hole Coalescence, *Phys. Rev. Lett.* **119**, 141101 (2017), [arXiv:1709.09660 \[gr-qc\]](#).
- [24] B. P. Abbott *et al.* (LIGO Scientific, Virgo), Tests of General Relativity with GW170817, *Phys. Rev. Lett.* **123**, 011102 (2019), [arXiv:1811.00364 \[gr-qc\]](#).
- [25] B. P. Abbott *et al.* (LIGO Scientific, Virgo), Tests of General Relativity with the Binary Black Hole Signals from the LIGO-Virgo Catalog GWTC-1, *Phys. Rev. D* **100**, 104036 (2019), [arXiv:1903.04467 \[gr-qc\]](#).
- [26] R. Abbott *et al.* (LIGO Scientific, Virgo), Tests of general relativity with binary black holes from the second LIGO-Virgo gravitational-wave transient catalog, *Phys. Rev. D* **103**, 122002 (2021), [arXiv:2010.14529 \[gr-qc\]](#).
- [27] R. Abbott *et al.* (LIGO Scientific, VIRGO, KAGRA), Tests of General Relativity with GWTC-3 (2021), [arXiv:2112.06861 \[gr-qc\]](#).
- [28] N. Yunes and F. Pretorius, Fundamental Theoretical Bias in Gravitational Wave Astrophysics and the Parameterized Post-Einsteinian Framework, *Phys. Rev. D* **80**, 122003 (2009), [arXiv:0909.3328 \[gr-qc\]](#).
- [29] T. G. F. Li, W. Del Pozzo, S. Vitale, C. Van Den Broeck, M. Agathos, J. Veitch, K. Grover, T. Sidery, R. Sturani, and A. Vecchio, Towards a generic test of the strong field dynamics of general relativity using compact binary coalescence, *Phys. Rev. D* **85**, 082003 (2012), [arXiv:1110.0530 \[gr-qc\]](#).
- [30] M. Agathos, W. Del Pozzo, T. G. F. Li, C. Van Den Broeck, J. Veitch, and S. Vitale, TIGER: A data analysis pipeline for testing the strong-field dynamics of general relativity with gravitational wave signals from coalescing compact binaries, *Phys. Rev. D* **89**, 082001 (2014), [arXiv:1311.0420 \[gr-qc\]](#).
- [31] A. K. Mehta, A. Buonanno, R. Cotesta, A. Ghosh, N. Sennett, and J. Steinhoff, Tests of general relativity with gravitational-wave observations using a flexible theory-independent method, *Phys. Rev. D* **107**, 044020 (2023), [arXiv:2203.13937 \[gr-qc\]](#).
- [32] B. P. Abbott *et al.* (LIGO Scientific, Virgo), Tests of general relativity with GW150914, *Phys. Rev. Lett.* **116**, 221101 (2016), [Erratum: *Phys. Rev. Lett.* **121**, 129902 (2018)], [arXiv:1602.03841 \[gr-qc\]](#).
- [33] M. Isi, K. Chatziioannou, and W. M. Farr, Hierarchical test of general relativity with gravitational waves, *Phys. Rev. Lett.* **123**, 121101 (2019), [arXiv:1904.08011 \[gr-qc\]](#).
- [34] P. Saini, S. A. Bhat, M. Favata, and K. G. Arun, Eccentricity-induced systematic error on parametrized tests of general relativity: Hierarchical Bayesian inference applied to a binary black hole population, *Phys. Rev. D* **109**, 084056 (2024), [arXiv:2311.08033 \[gr-qc\]](#).
- [35] A. Buonanno and T. Damour, Effective one-body approach to general relativistic two-body dynamics, *Phys. Rev. D* **59**, 084006 (1999), [arXiv:gr-qc/9811091](#).
- [36] A. Buonanno and T. Damour, Transition from inspiral to plunge in binary black hole coalescences, *Phys. Rev. D* **62**, 064015 (2000), [arXiv:gr-qc/0001013](#).
- [37] Y. Pan, A. Buonanno, M. Boyle, L. T. Buchman, L. E. Kidder, H. P. Pfeiffer, and M. A. Scheel, Inspiral-merger-ringdown multipolar waveforms of nonspinning black-hole binaries using the effective-one-body formalism, *Phys. Rev. D* **84**, 124052 (2011), [arXiv:1106.1021 \[gr-qc\]](#).
- [38] A. Pai and K. G. Arun, Singular value decomposition in parametrised tests of post-Newtonian theory, *Class. Quant. Grav.* **30**, 025011 (2013), [arXiv:1207.1943 \[gr-qc\]](#).
- [39] M. Saleem, S. Datta, K. G. Arun, and B. S. Sathyaprakash, Parametrized tests of post-Newtonian theory using principal component analysis, *Phys. Rev. D* **105**, 084062 (2022), [arXiv:2110.10147 \[gr-qc\]](#).
- [40] S. Datta, M. Saleem, K. G. Arun, and B. S. Sathyaprakash, Multiparameter tests of general relativity using a principle component analysis with next-generation gravitational-wave detectors, *Phys. Rev. D* **109**, 044036 (2024), [arXiv:2208.07757 \[gr-qc\]](#).
- [41] J. M. Dickey, The Weighted Likelihood Ratio, Linear Hypotheses on Normal Location Parameters, *The Annals of Mathematical Statistics* **42**, 204 (1971).
- [42] M. Isi, W. M. Farr, and K. Chatziioannou, Comparing Bayes factors and hierarchical inference for testing general relativity with gravitational waves, *Phys. Rev. D* **106**, 024048 (2022), [arXiv:2204.10742 \[gr-qc\]](#).
- [43] E. Payne, M. Isi, K. Chatziioannou, and W. M. Farr,

- Fortifying gravitational-wave tests of general relativity against astrophysical assumptions, *Phys. Rev. D* **108**, 124060 (2023), [arXiv:2309.04528 \[gr-qc\]](#).
- [44] E. Payne, M. Isi, K. Chatziioannou, L. Lehner, Y. Chen, and W. M. Farr, The curvature dependence of gravitational-wave tests of General Relativity (2024), [arXiv:2407.07043 \[gr-qc\]](#).
- [45] H. Zhong, M. Isi, K. Chatziioannou, and W. M. Farr, Multidimensional hierarchical tests of general relativity with gravitational waves, *Phys. Rev. D* **110**, 044053 (2024), [arXiv:2405.19556 \[gr-qc\]](#).
- [46] T. Regge and J. A. Wheeler, Stability of a Schwarzschild singularity, *Phys. Rev.* **108**, 1063 (1957).
- [47] T. Damour and A. Nagar, Final spin of a coalescing black-hole binary: An Effective-one-body approach, *Phys. Rev. D* **76**, 044003 (2007), [arXiv:0704.3550 \[gr-qc\]](#).
- [48] T. Damour and A. Nagar, An Improved analytical description of inspiralling and coalescing black-hole binaries, *Phys. Rev. D* **79**, 081503 (2009), [arXiv:0902.0136 \[gr-qc\]](#).
- [49] L. Pompili *et al.*, Laying the foundation of the effective-one-body waveform models SEOBNRv5: Improved accuracy and efficiency for spinning nonprecessing binary black holes, *Phys. Rev. D* **108**, 124035 (2023), [arXiv:2303.18039 \[gr-qc\]](#).
- [50] L. S. Finn, Detection, measurement and gravitational radiation, *Phys. Rev. D* **46**, 5236 (1992), [arXiv:gr-qc/9209010](#).
- [51] C. Cutler and M. Vallisneri, LISA detections of massive black hole inspirals: Parameter extraction errors due to inaccurate template waveforms, *Phys. Rev. D* **76**, 104018 (2007), [arXiv:0707.2982 \[gr-qc\]](#).
- [52] Q. Hu and J. Veitch, Accumulating Errors in Tests of General Relativity with Gravitational Waves: Overlapping Signals and Inaccurate Waveforms, *Astrophys. J.* **945**, 103 (2023), [arXiv:2210.04769 \[gr-qc\]](#).
- [53] B. Seymour, J. Golomb, and Y. Chen, Inspiral Tests of General Relativity and Waveform Geometry (2024), in progress.
- [54] R. Magee, M. Isi, E. Payne, K. Chatziioannou, W. M. Farr, G. Pratten, and S. Vitale, Impact of selection biases on tests of general relativity with gravitational-wave inspirals, *Phys. Rev. D* **109**, 023014 (2024), [arXiv:2311.03656 \[gr-qc\]](#).
- [55] E. Thrane and C. Talbot, An introduction to Bayesian inference in gravitational-wave astronomy: parameter estimation, model selection, and hierarchical models, *Publ. Astron. Soc. Austral.* **36**, e010 (2019), [Erratum: *Publ.Astron.Soc.Austral.* 37, e036 (2020)], [arXiv:1809.02293 \[astro-ph.IM\]](#).
- [56] M. Fishbach, D. E. Holz, and W. M. Farr, Does the Black Hole Merger Rate Evolve with Redshift?, *Astrophys. J. Lett.* **863**, L41 (2018), [arXiv:1805.10270 \[astro-ph.HE\]](#).
- [57] C. Talbot and E. Thrane, Measuring the binary black hole mass spectrum with an astrophysically motivated parameterization, *Astrophys. J.* **856**, 173 (2018), [arXiv:1801.02699 \[astro-ph.HE\]](#).
- [58] R. Abbott *et al.* (KAGRA, VIRGO, LIGO Scientific), Population of Merging Compact Binaries Inferred Using Gravitational Waves through GWTC-3, *Phys. Rev. X* **13**, 011048 (2023), [arXiv:2111.03634 \[astro-ph.HE\]](#).
- [59] L. Sampson, N. Cornish, and N. Yunes, Gravitational Wave Tests of Strong Field General Relativity with Binary Inspirals: Realistic Injections and Optimal Model Selection, *Phys. Rev. D* **87**, 102001 (2013), [arXiv:1303.1185 \[gr-qc\]](#).
- [60] J. Meidam *et al.*, Parametrized tests of the strong-field dynamics of general relativity using gravitational wave signals from coalescing binary black holes: Fast likelihood calculations and sensitivity of the method, *Phys. Rev. D* **97**, 044033 (2018), [arXiv:1712.08772 \[gr-qc\]](#).
- [61] T. Damour, B. R. Iyer, and A. Nagar, Improved resummation of post-Newtonian multipolar waveforms from circularized compact binaries, *Phys. Rev. D* **79**, 064004 (2009), [arXiv:0811.2069 \[gr-qc\]](#).
- [62] A. Buonanno, Y. Pan, H. P. Pfeiffer, M. A. Scheel, L. T. Buchman, and L. E. Kidder, Effective-one-body waveforms calibrated to numerical relativity simulations: Coalescence of non-spinning, equal-mass black holes, *Phys. Rev. D* **79**, 124028 (2009), [arXiv:0902.0790 \[gr-qc\]](#).